

Reaction $\bar{p}p \rightarrow \bar{\Lambda}\Lambda$ in the meson-exchange picture

J. Haidenbauer

Institut für Kernphysik, Forschungszentrum Jülich GmbH, D-5170 Jülich, Germany
and Department of Physics and Mathematical Physics, The University of Adelaide, Adelaide, South Australia 5001, Australia

T. Hippchen, K. Holinde, B. Holzenkamp, V. Mull, and J. Speth

Institut für Kernphysik, Forschungszentrum Jülich GmbH, D-5170 Jülich, Germany

(Received 15 July 1991)

A study of the strangeness production process $\bar{p}p \rightarrow \bar{\Lambda}\Lambda$ at threshold and intermediate energies has been performed doing a full coupled-channel ($\bar{p}p, \bar{\Lambda}\Lambda$) calculation. The elastic part of the $\bar{p}p$ and $\bar{\Lambda}\Lambda$ interactions has been derived from a one-boson-exchange version of the Bonn NN potential and a corresponding extension to the hyperon-nucleon case whereas the annihilation part is taken into account by introducing suitable optical potentials. The transition interaction between $\bar{p}p$ and $\bar{\Lambda}\Lambda$ is based on K - and K^* -meson exchange. A reasonably good description of empirical cross sections as well as polarization data is achieved. It is demonstrated that the results are quite sensitive even to short-range modifications of the channel interactions. We also compare our model with other approaches and suggest a new experiment which would be able to check the very different predictions of the meson-exchange and constituent quark model, respectively.

PACS number(s): 25.43.+t, 13.75.Cs, 21.30.+j

I. INTRODUCTION

In the last few years considerable attention has been paid to the study of antilambda-lambda ($\bar{\Lambda}\Lambda$) pair creation in antiproton-proton ($\bar{p}p$) scattering. These efforts were stimulated by the expectation that close to the production threshold the reaction mechanism should be relatively simple since only a few partial waves contribute. Consequently, it is hoped that this reaction might provide conclusive information about the strong-interaction mechanism leading to strangeness formation.

At present, there exist essentially two pictures to describe this strangeness formation. The first one is the conventional (t -channel) boson-exchange model using not only K mesons [1,2] but in some cases K^* (892, $J^P=1^-$) [3-6] and also K_2^* (1430, $J^P=2^+$) [5]. The second one is based on the constituent quark model describing $\bar{s}s$ production from $\bar{u}u$ annihilation [7-12].

The work presented here relies on the conventional meson-exchange framework. For the transition interaction, we include not only K but also K^* exchange with vertex parameters, completely consistent with our hyperon-nucleon interaction model [13]. The inclusion of K^* exchange in the hyperon-nucleon system is dictated by analogy to the NN system, in which ρ exchange has proven its outstanding importance.

Since in the $\bar{p}p \rightarrow \bar{\Lambda}\Lambda$ transition K and K^* exchange add up in the tensor channel, but have opposite sign in the central channel, our model for the transition interaction has an extremely strong tensor force (especially since we do not cut off the potential in the inner region), but a rather weak central force. This characteristic feature is much more pronounced than in a model with K exchange only and even opposite to the constituent quark model in which the tensor transitions are strongly suppressed (3P_0 version [9]) or even forbidden (3S_1 version). Therefore, the physics involved in our ($K+K^*$) transition potential

is completely different from the transition mechanism connected with the constituent quark model: Since in the meson-exchange transition potential the tensor force is by far the strongest component, the spin-triplet configurations have to flip the spin in the transition between the $\bar{p}p$ and $\bar{\Lambda}\Lambda$ systems, whereas this is essentially not the case for the quark models.

In spite of the strongly different characteristics of the transition process in the meson-exchange and quark-gluon models, both scenarios seem to describe the present experimental data with roughly the same quality. One reason is that the $\bar{p}p \rightarrow \bar{\Lambda}\Lambda$ process is strongly influenced by both initial- and final-state interactions. Whereas the $\bar{p}p$ interaction can, at least to some extent, be constrained by available empirical $\bar{p}p$ scattering data in the relevant energy range, no direct empirical information exists for the $\bar{\Lambda}\Lambda$ interaction. Therefore, a variety of models for the basic transition mechanism can be made to fit the $\bar{p}p \rightarrow \bar{\Lambda}\Lambda$ data, provided appropriately adjusted final-state interactions are employed.

The elastic part of the $\bar{p}p$ interaction is taken to be the G -parity transform of an energy-independent one-boson-exchange (OBE) version (OBEPF of Ref. [14]) of the Bonn NN potential [15]. Likewise, the corresponding $\bar{\Lambda}\Lambda$ interaction is derived from a $\bar{\Lambda}\Lambda$ potential, which, in turn, is obtained from our hyperon-nucleon potential [13]. We stress that no *ad hoc* modification of the inner part of any of these meson-exchange interactions has been introduced. Not only coupling constants, but also form factor parameters have been taken over from the nucleon-nucleon and hyperon-nucleon sector (with one exception to be discussed below). We feel that such a consistent treatment of various hadronic reactions is important in order to really explore the limits of the conventional picture.

For the moment the annihilation part of both the $\bar{p}p$ and $\bar{\Lambda}\Lambda$ interaction is parametrized in terms of simple spin-, isospin-, and energy-independent optical potential

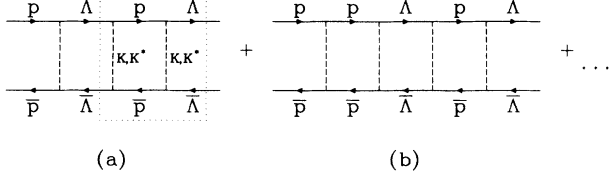


FIG. 1. Processes included in our coupled-channel framework in addition to the Born term. In (a) we show within the dotted area coupled-channel contributions which have been included in Ref. [2] in a phenomenological way.

of Gaussian form. In case of $\bar{p}p$, the occurring parameters have been independently fixed by adjusting them to $\bar{p}p$ scattering data in the relevant energy range; corresponding parameters for $\bar{\Lambda}\Lambda$ are the only free parameters in the present work, to be adjusted to the $\bar{p}p \rightarrow \bar{\Lambda}\Lambda$ data.

In principle, it would be desirable to describe the annihilation processes in the same microscopic meson-exchange framework, which, however, would be extremely complicated and surely beyond the scope of the present paper. Note, however, that the longer-ranged elastic and transition part is described consistently in our model. This is usually not the case in present quark-model calculations.

In this paper we go beyond the distorted-wave Born-approximation (DWBA) approach by doing a full coupled-channel ($\bar{p}p, \bar{\Lambda}\Lambda$) calculation. We thus include automatically processes such as those shown in Fig. 1. In the DWBA calculation of Ref. [2], the process in Fig. 1(a) has been qualitatively taken into account by adding a phenomenological piece to the $\bar{\Lambda}\Lambda$ interaction with the range of two kaon masses and found to be quite important.

In the next section, we will briefly outline the formalism and specify the various channel potentials. In Sec. III we present and discuss the numerical results and compare them with other approaches. The paper ends with a short summary and outlook.

II. MODEL

A. Coupled-channel formalism

We start by defining channel matrix elements for the potential, $V^{i'i}(\mathbf{q}', \mathbf{q}, z)$, and for the scattering amplitude, $T^{i'i}(\mathbf{q}', \mathbf{q}, z)$. Here z denotes the starting energy and \mathbf{q}' (\mathbf{q}) the c.m.s. (center-of-mass-system) relative momentum in the final (initial) channel. Note that the latter are different in different channels and that the spin and isospin dependence is suppressed for simplicity. i' (i) characterizes the outgoing (incoming) channel with $i=1$ for $\bar{p}p$ and $i=2$ for $\bar{\Lambda}\Lambda$. Using these definitions, the T -matrix equation to be solved reads

$$T^{i'i}(\mathbf{q}', \mathbf{q}, z) = V^{i'i}(\mathbf{q}', \mathbf{q}, z) + \sum_{i''=1,2} \int d^3q'' V^{i'i''}(\mathbf{q}', \mathbf{q}'', z) \times \frac{1}{z - E_{q''}^{(i'')} + i\epsilon} T^{i''i}(\mathbf{q}'', \mathbf{q}, z). \quad (2.1)$$

Here $E_{q''}^{(i'')}$ denotes the intermediate energy in channel i'' , i.e.,

$$E_{q''}^{(1)} = E_{q''}(p) + E_{q''}(\bar{p}), \quad (2.2)$$

$$E_{q''}^{(2)} = E_{q''}(\Lambda) + E_{q''}(\bar{\Lambda}).$$

This equation can be written in matrix form:

$$T(\mathbf{q}', \mathbf{q}, z) = V(\mathbf{q}', \mathbf{q}, z) + \int d^3q'' V(\mathbf{q}', \mathbf{q}'', z) G_0(q'', z) T(\mathbf{q}'', \mathbf{q}, z), \quad (2.3)$$

with the definitions

$$G_0(q'', z) = \begin{pmatrix} 1/(z - E_{q''}^{(1)} + i\epsilon) & 0 \\ 0 & 1/(z - E_{q''}^{(2)} + i\epsilon) \end{pmatrix}, \quad (2.4a)$$

$$V(\mathbf{q}', \mathbf{q}, z) = \begin{pmatrix} V^{11}(\mathbf{q}', \mathbf{q}, z) & V^{12}(\mathbf{q}', \mathbf{q}, z) \\ V^{21}(\mathbf{q}', \mathbf{q}, z) & V^{22}(\mathbf{q}', \mathbf{q}, z) \end{pmatrix}, \quad (2.4b)$$

and similarly for $T(\mathbf{q}', \mathbf{q}, z)$.

Based on these T -matrix amplitudes, it is then straightforward to evaluate the scattering observables such as differential cross sections, polarizations, spin-correlation parameters, etc. With the usual parametrization of the spin-scattering matrix (see, e.g., Appendix C of Ref. [13]), one obtains the following results:

differential cross section,

$$\frac{d\sigma}{d\Omega} = I_0 = \frac{q'}{q} \frac{1}{2} (|a|^2 + |b|^2 + |c|^2 + |d|^2 + |e|^2 + |g|^2), \quad (2.5)$$

polarizations,

$$P_y^\Lambda = \frac{q'}{q} \frac{1}{I_0} [\text{Re}(ae^*) + \text{Im}(dg^*)] = P_y^{\bar{\Lambda}}, \quad (2.6)$$

spin-correlation parameters,

$$C_{xx} = -\frac{q'}{q} \frac{1}{I_0} [\text{Re}(ad^* + bc^*) + \text{Im}(ge^*)],$$

$$C_{yy} = \frac{q'}{q} \frac{1}{2I_0} (|a|^2 - |b|^2 - |c|^2 + |d|^2 + |e|^2 + |g|^2), \quad (2.7)$$

$$C_{zz} = \frac{q'}{q} \frac{1}{I_0} [\text{Re}(ad^* - bc^*) + \text{Im}(ge^*)],$$

$$C_{xz} = -\frac{q'}{q} \frac{1}{I_0} [\text{Re}(ag^*) + \text{Im}(ed^*)].$$

Note that because of charge-conjugation invariance, $C_{zx} = C_{xz}$, and because of parity conservation, $C_{xy} = C_{yx} = C_{yz} = C_{zy} = 0$. The singlet fraction, which is of interest in these studies, is given by

$$F_S = \frac{1}{4} (1 + C_{xx} - C_{yy} + C_{zz}). \quad (2.8)$$

B. Channel interactions

1. V^{11} : $\bar{p}p \rightarrow \bar{p}p$

We now have to specify the various channel interactions V^{ii} , which serve as input for the scattering equation (2.3). Recently, we have presented [16] $\bar{N}N$ potentials in which the elastic part is given by the G -parity transform of the full Bonn potential [15], whereas the annihilation part is either parametrized in terms of a simple optical potential or microscopically derived in a consistent baryon-exchange model, including the dominant two-meson annihilation channels. Open parameters have been adjusted to the (low-energy) $\bar{p}p$ data.

However, these potentials cannot be blindly used as input for the present case since the $\bar{p}p$ scattering energy is now much higher. In fact, the required energy for the production of a $\bar{\Lambda}\Lambda$ pair is larger than the pion-production threshold energy in the NN system, a region which the Bonn NN potential [15] is not applicable to and was not designed for. (Note that the same is true for the Nijmegen [17] and Paris [18] potentials.) Completely in line with comparable calculations, we ignore this problem and start from a simple, energy-independent one-boson-exchange NN potential (OBEPF) [14], which describes sufficiently well the low-energy NN data and can be easily extended to higher energies. In a first step (A), we add to its G -parity transform a spin-, isospin-, and energy-independent optical potential of Gaussian form, which reads, in coordinate space (the actual calculations are done in momentum space, i.e., with the Fourier transform),

$$\text{A: } V_{\text{opt}}^{\bar{p}p}(r) = (U_c + iW_c) e^{-r^2/2r_0^2}. \quad (2.9)$$

Note that we also include a real piece since annihilation processes to be effectively taken into account by this expression contain likewise not only an imaginary, but also a real part.

In principle, the open parameters of $V_{\text{opt}}^{\bar{p}p}$ can only be determined, together with additional parameters in the diagonal $\bar{\Lambda}\Lambda$ interaction, by solving the full T -matrix equation (2.3) and comparing with empirical data in $\bar{p}p \rightarrow \bar{p}p$, $\bar{\Lambda}\Lambda$. Fortunately, the effect of the $\bar{\Lambda}\Lambda$ channel on the diagonal $\bar{p}p$ T matrix can be safely neglected since the branching ratio $\bar{p}p \rightarrow \bar{\Lambda}\Lambda$ is extremely small. Therefore, U_c , W_c , and r_0 can be determined independently from the $\bar{\Lambda}\Lambda$ channel by solving the much simpler uncoupled equation

$$\begin{aligned} T^{11}(\mathbf{q}', \mathbf{q}, z) &= V^{11}(\mathbf{q}', \mathbf{q}, z) \\ &+ \int d^3q'' V^{11}(\mathbf{q}', \mathbf{q}'', z) \\ &\times \frac{1}{z - E_{q''}^{(1)} + i\epsilon} T^{11}(\mathbf{q}'', \mathbf{q}, z), \end{aligned} \quad (2.10)$$

and comparing the resulting observables with empirical $\bar{p}p$ data in the required energy range. The adjusted parameters are given in Table I, together with those of two low-energy $\bar{N}N$ models. The first one [A(OBEF) [19]] is based on exactly the same NN potential (OBEPF, Ref. [14]) used here, whereas the second set (taken from Ref. [16]) belongs to the energy-dependent OBE version (OBEPT) of Ref. [15]. Obviously, the parameters depend considerably on the energy range. Such an energy dependence of the annihilation part is not surprising and completely in line with microscopic models based, e.g., on baryon exchange. Indeed, the imaginary part should go up with energy since more and more annihilation channels open up.

Figure 2 demonstrates that the integrated cross-section data can be quantitatively reproduced; also a reasonable description of the empirical data is obtained for the (elastic) differential cross sections (see Fig. 3), whereas the polarization is consistently too low, as shown in Fig. 4.

An important point of this paper will be the study of the sensitivity of the $\bar{p}p \rightarrow \bar{\Lambda}\Lambda$ results to slight modifications of the $\bar{p}p$ interaction in the inner region only. Therefore, we have constructed a second model (B) in which we keep the longer-ranged G -parity transform exactly the same and allow only for an additional spin-orbit term in the optical potential (whose presence is anyhow suggested from microscopic calculations of the annihilation part):

$$\text{B: } V_{\text{opt}}^{\bar{p}p}(r) = [U_c + iW_c + (U_{LS} + iW_{LS})\mathbf{L}\cdot\mathbf{S}] e^{-r^2/2r_0^2}. \quad (2.11)$$

The chosen parameters are also given in Table I. As seen from Figs. 2 and 3, the new model provides for essentially the same integrated and differential cross sections; however, as expected, the inclusion of the spin-orbit term in $V_{\text{opt}}(B)$ increases the resulting polarizations drastically, being now more in line with experiment (cf. Fig. 4).

We did not try to improve the polarization results further, e.g., by adding more terms in the optical potential and/or making the parameters energy dependent. Rath-

TABLE I. Parameters of the phenomenological optical potential in the $\bar{p}p$ channel, for two different models described in the text, and, for comparison, of the low-energy models A(OBEF) [A(OBE)] of Ref. [19] ([16]).

	A	B	A(OBEF)	A(OBE)
U_c	+788 MeV	-1260 MeV	-1181 MeV	-1260 MeV
W_c	-2756 MeV	-4331 MeV	-945 MeV	-1575 MeV
U_{LS}		-1575 MeV		
W_{LS}		+394 MeV		
r_0	0.46 fm	0.40 fm	0.39 fm	0.40 fm

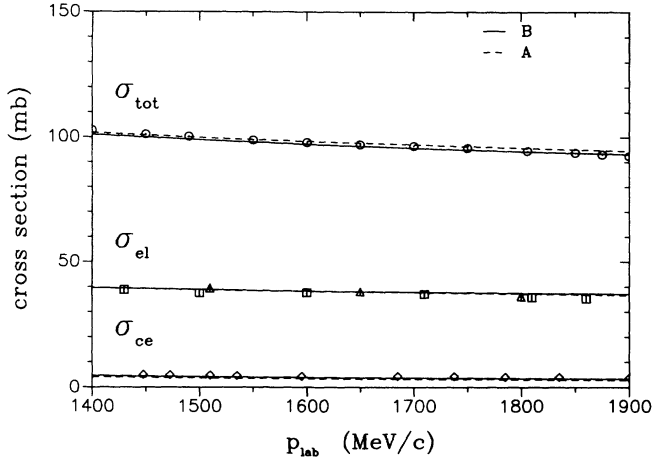


FIG. 2. $\bar{p}p$ total, integrated elastic, and charge-exchange cross sections predicted by our models A (dashed) and B (solid) for the initial-state interaction. Experimental data are from Refs. [20] (circles), [21] (squares), [22] (triangles), and [23] (diamonds).

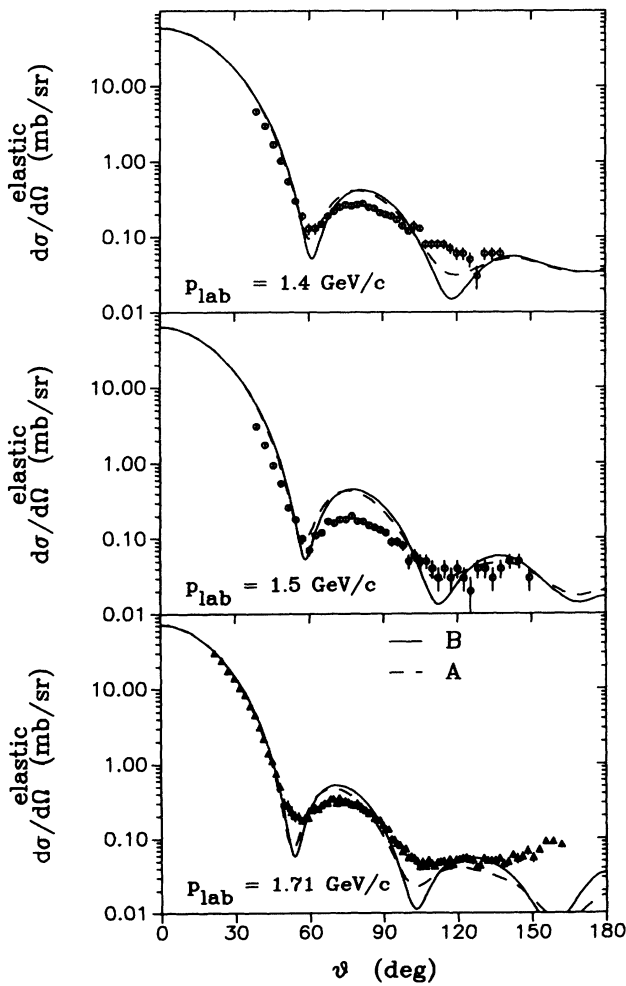


FIG. 3. $\bar{p}p$ elastic differential cross section. Same description of the curves as in Fig. 2. Experimental data are from Refs. [24] (circles) and [25] (triangles).

er, we feel that future efforts should go more in the direction of improving the theoretical basis of the $\bar{p}p$ model in this energy range, for the annihilation as well as the elastic part. Nevertheless, the models presented here should provide a reasonable overall description of $\bar{p}p$ distortions in the $\bar{p}p \rightarrow \bar{\Lambda}\Lambda$ reaction.

2. V^{22} : $\bar{\Lambda}\Lambda \rightarrow \bar{\Lambda}\Lambda$

The specifications of the diagonal $\bar{\Lambda}\Lambda$ interaction is done in close analogy to the $\bar{p}p$ case. In the simple OBE picture, the elastic part is essentially given by the isospin-zero σ and ω exchanges. Both coupling constants as well as the $\Lambda\Lambda\omega$ cutoff mass are taken the same as predetermined from our hyperon-nucleon model A (see Ref. [13]). We could not use the extremely low value of 1 GeV for the $\Lambda\Lambda\sigma$ cutoff mass used in Ref. [13]. We have chosen 1.7 GeV, which anyhow seems to be more realistic. Moreover, part of the required increase is probably needed to compensate for the omission of the $\bar{\Lambda}\Sigma$ and $\bar{\Sigma}\Sigma$

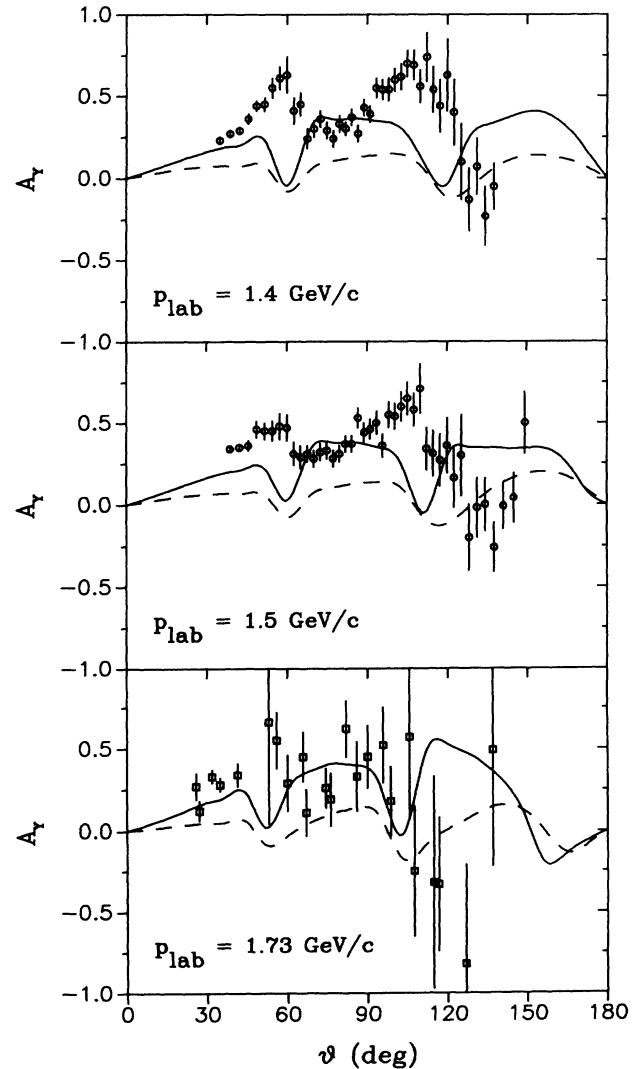


FIG. 4. $\bar{p}p$ elastic analyzing powers. Same description of the curves as in Fig. 2. Experimental data are from Refs. [25] (circles) and [26] (squares).

TABLE II. Ingredients of various models discussed in the present work.

	$\bar{p}p$ model	$\Lambda_{N\Lambda K^*}$ (GeV)
I	B	2.2
II	B	1.5
III	A	1.5

channels in the present calculation. Note that, in contrast to the former $\bar{p}p$ case, the $\bar{\Lambda}\Lambda$ interaction is now required at rather low energies, i.e., in a region consistent with present hyperon-nucleon studies.

The shorter-ranged annihilation part is again parametrized by an optical potential of Gaussian form; however, we now include also a tensor-type term, which considerably improves the resulting description of $\bar{p}p \rightarrow \bar{\Lambda}\Lambda$ data:

$$V_{\text{opt}}^{\bar{\Lambda}\Lambda} = [U_c + iW_c + (U_{LS} + iW_{LS})\mathbf{L}\cdot\mathbf{S} + (U_t + iW_t)\sigma_{\Lambda}\cdot\mathbf{r}\sigma_{\bar{\Lambda}}\cdot\mathbf{r}]e^{-r^2/2r_0^2}. \quad (2.12)$$

The various strength parameters and common range are fitted to the empirical $\bar{p}p \rightarrow \bar{\Lambda}\Lambda$ data. Corresponding values will be shown and discussed in the next section.

3. V^{21} : $\bar{p}p \rightarrow \bar{\Lambda}\Lambda$

As mentioned already in the Introduction, the nondiagonal potential matrix elements are based on K^* as well as K exchange. Corresponding expressions as well as parameter values (coupling constants, cutoff masses) are taken in precise consistency with our hyperon-nucleon model A (see Ref. [13]). Since the $N\Lambda K^*$ cutoff mass (2.2 GeV) appears to be rather high, we used alternatively the value of 1.5 GeV. Since this change influences the region inside 0.8 fm only, it will give an impression of how sensitive or insensitive the results are to phenomenological regularization procedures such as smooth extrapolation to zero distance.

III. RESULTS

A. Parameters

Our first model (I) is based on central plus spin-orbit interaction in the phenomenological annihilation potential (B) together with a cutoff mass Λ of 2.2 GeV at the $N\Lambda K^*$ vertex, fixed by our hyperon-nucleon model (A) of Ref. [13]. In order to study the sensitivity of the results

to variations in the short-range part of the interactions, we will present and discuss the results of two further models whose ingredients are summarized in Table II. The results of model (I) are considered as the final results of our calculation.

For all models the seven open parameters in the short-ranged $\bar{\Lambda}\Lambda$ annihilation interaction [Eq. (2.12)] have been adjusted to the $\bar{p}p \rightarrow \bar{\Lambda}\Lambda$ data. The resulting values are given in Table III. Obviously, they depend considerably on the kind of short-range modification applied. This fact suggests already at this stage that an unambiguous determination of the $\bar{\Lambda}\Lambda$ interaction will be extremely hard, even if the (longer-ranged) elastic part is kept fixed. This will become more transparent when we look at some of the resulting observables in the $\bar{\Lambda}\Lambda$ channel at the end of this section.

B. Near threshold

Figure 5 shows the resulting $\bar{p}p \rightarrow \bar{\Lambda}\Lambda$ total cross section near threshold; obviously, all variants provide almost identical results, in good agreement with the empirical data. Concerning the differential cross sections, shown in Fig. 6, all models can reproduce the trend of the data. As demonstrated in Fig. 7(a), all our three model predictions for S and P waves agree quite well with the “experimental” S - and P -wave contributions determined from the empirical decomposition $\sigma_{\text{tot}} = 1.51\epsilon^{1/2} + 0.26\epsilon^{3/2}$ [26], whereas the models of Kohno and Weise (KW, Ref. [1]) and LaFrance and Loiseau (LL, Ref. [2]) show considerable deviations, in opposite directions [Fig. 7(b)].

Figure 8 shows the resulting polarizations at threshold, which are in good agreement with the data. Note that our models predict a zero crossing at $p_{\text{lab}} = 1445.3$ MeV, which happens at somewhat larger backward angles than for both models KW and LL.

C. Higher energies

We start again by showing in Fig. 9 the resulting total $\bar{p}p \rightarrow \bar{\Lambda}\Lambda$ cross sections, up to a nucleon laboratory momentum of 1.9 GeV. Also our model variants provide a good description of the empirical situation. Furthermore, we show differential cross sections (Fig. 10) and polarizations (Fig. 11) at those energies where experimental data exist or will be available soon [25,30]. The general trend of the data is well reproduced over the whole energy range.

TABLE III. Parameters of the phenomenological optical potential in the $\bar{\Lambda}\Lambda$ channel, for three different models described in the text.

	I	II	III
U_c	-1142 MeV	-1181 MeV	-1166 MeV
W_c	-1142 MeV	-787 MeV	-473 MeV
U_{LS}	+236 MeV	+158 MeV	+236 MeV
W_{LS}	+79 MeV	-315 MeV	-630 MeV
U_t	-1260 MeV fm ⁻²	-1418 MeV fm ⁻²	-2048 MeV fm ⁻²
W_t	+40 MeV fm ⁻²	+40 MeV fm ⁻²	-158 MeV fm ⁻²
r_0	0.34 fm	0.30 fm	0.25 fm

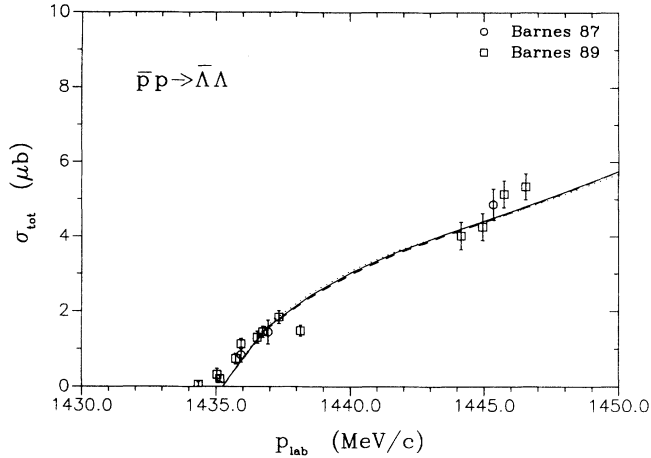


FIG. 5. Total $\bar{p}p \rightarrow \bar{\Lambda}\Lambda$ cross sections near threshold, predicted by our models I (solid), II (dashed), and III (dotted). Experimental data are from Refs. [27] (circles) and [28] (squares). We exhibit in most of the following figures the results of three models to shed light on the sensitivity of results to variations in parameters. However, we stress that physical significance should be attached only to the results of model I (solid line).

Figure 12 (13) shows the $\bar{p}p \rightarrow \bar{\Lambda}\Lambda$ spin-correlation coefficients C_{ij} at $p_{\text{lab}} = 1.546 \text{ GeV}/c$ ($1.695 \text{ GeV}/c$). All our models provide similar results, in some cases yielding sizable discrepancies to the data and to the model predictions of LL. The singlet fraction defined in Eq. (2.8) is shown, too. All the models, in agreement with experiment, predict the $\bar{\Lambda}\Lambda$ state to be produced mainly in the triplet state.

From the results presented so far, the reader might have come to the erroneous conclusion that the $\bar{p}p \rightarrow \bar{\Lambda}\Lambda$ observables depend only slightly on modifications in the short-ranged annihilation part of the initial-state interaction (difference between models II and III) and even less on modifications in the inner part of the transition interaction (difference between models I and II). However, as seen from Table III, the $\bar{\Lambda}\Lambda$ optical-model parameters had to be considerably readjusted in order to obtain comparable results in the $\bar{p}p \rightarrow \bar{\Lambda}\Lambda$ channel. Indeed, if we keep these parameters the same as in model I, the modifications lead in both cases to sizable changes of the total $\bar{\Lambda}\Lambda$ cross section, over the whole energy range, as shown in Table IV.

D. Discussion and comparison with other models

We start this section by giving in Table V the partial cross sections at $p_{\text{lab}} = 1546 \text{ MeV}/c$. Obviously, for all our models the reaction is dominated by transitions which change the orbital angular momentum by two units: $L_{\bar{\Lambda}\Lambda} = L_{\bar{p}p} - 2$. Qualitatively, a similar result has been obtained by the Nijmegen group [4], shown also in Table V, although there are differences in detail: For example, the dominance of the 3F_2 - 3P_2 transition is even more pronounced in our case; furthermore, the role of 3P_0 and 3P_1 is interchanged. At this energy the four largest contributions are 3F_2 - 3P_2 , 3G_3 - 3D_3 , 3P_0 , and 3D_1 - 3S_1 ;

their energy dependence is plotted in Fig. 14 for model I. Obviously, the 3F_2 - 3P_2 transition saturates at higher energies so that at $p_{\text{lab}} \gtrsim 1620 \text{ MeV}/c$ the 3G_3 - 3D_3 transition, playing only a minor role in low-energy NN scattering, becomes even larger. This is not unexpected because at larger energies higher partial waves become increasingly more important.

It is important to realize that the dominance of the tensor force in the transition between the $\bar{p}p$ and $\bar{\Lambda}\Lambda$ system is *the* specific feature of our meson-exchange model including K as well as K^* mesons. These two mesons play the same role in the ΛN and ΣN potentials [13] as π and ρ in the usual NN potential. In all cases we obtain central and tensor components: The central components add coherently (giving rise, e.g., to the strong g'_0 Landau parameter in the nucleon-nucleon case), whereas the tensor components have opposite sign. Therefore, the ρ and K^* mesons reduce the strong tensor forces coming from π -

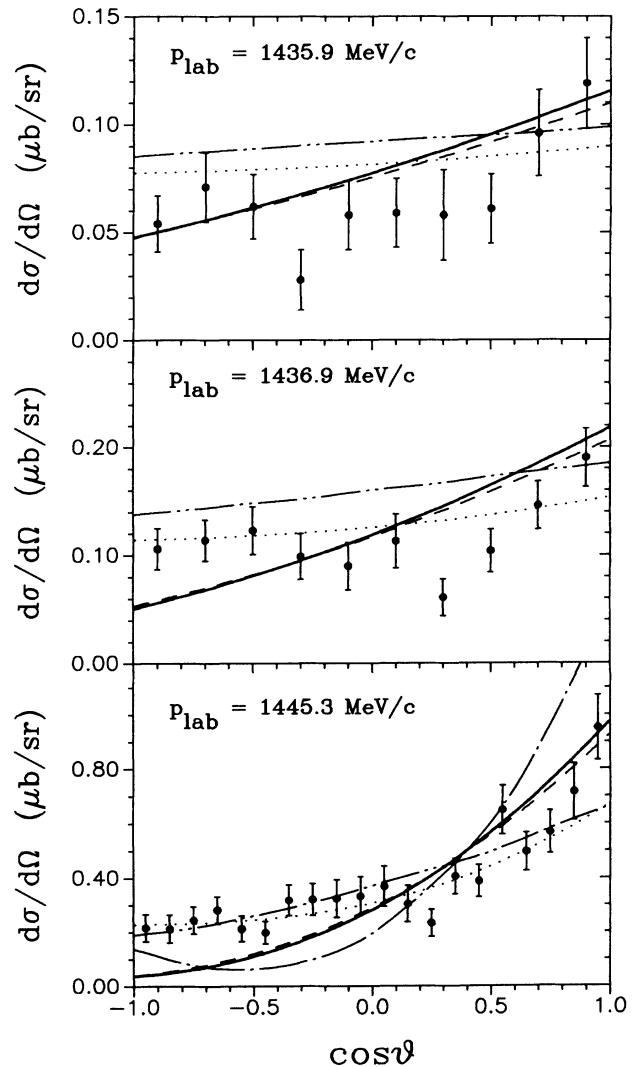


FIG. 6. Differential $\bar{p}p \rightarrow \bar{\Lambda}\Lambda$ cross sections near threshold. In addition to our results (solid, dotted, and dashed) specified in Fig. 5, predictions of the Kohno-Weise model [1] (dash-dotted) and LaFrance-Loiseau [2] (dash-double dotted) are shown in the lower part. Experimental data are from Ref. [29].

and K -meson exchange, respectively. If we consider corresponding baryon-antibaryon systems, the signs of the π - and K -meson contributions are changed. For that reason, in our model for $\bar{p}p \rightarrow \bar{\Lambda}\Lambda$, the central part of the transition potential is weak since the K and K^* contributions cancel each other to a large extent, whereas the tensor part is quite strong because the K and K^* contributions have the same sign. The situation is completely different for transition potentials based on the constituent quark model: For the 3P_0 version (see Fig. 3 of Ref. [9]), the tensor force is rather weak; it even vanishes for the 3S_1 case. Thus spin-flip transitions, which are dominant in our meson-exchange model, are either completely forbidden (3S_1) or at least strongly suppressed (3P_0) in quark-model calculations. Although the completely different physics should have some impact on the numerical results, the basic qualitative features of the $\bar{p}p \rightarrow \bar{\Lambda}\Lambda$ process, namely, the dominance of spin-triplet configurations and the P -wave dominance at the $\bar{\Lambda}\Lambda$ threshold, are nevertheless supplied by both pictures.

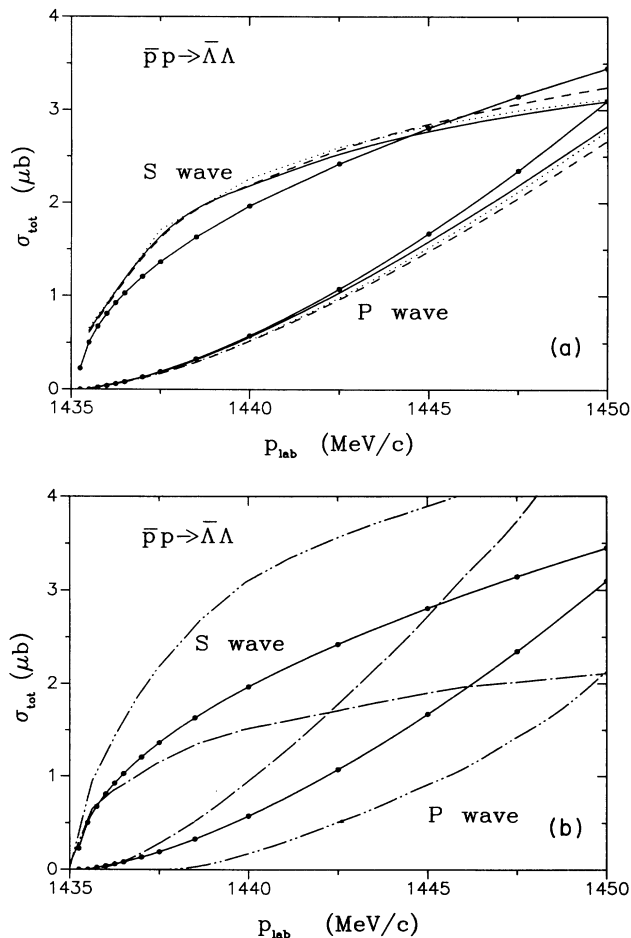


FIG. 7. (a) S - and P -wave contributions to the total $\bar{p}p \rightarrow \bar{\Lambda}\Lambda$ cross section near threshold calculated within our three different models. Same description of the curves as in Fig. 5. The dots connected by a solid line result from an empirical decomposition [28]; see text. (b) The results of Kohno-Weise [1] (dash-dotted) and of LaFrance-Loiseau [2] (dash-double dotted) in comparison with the empirical data [28].

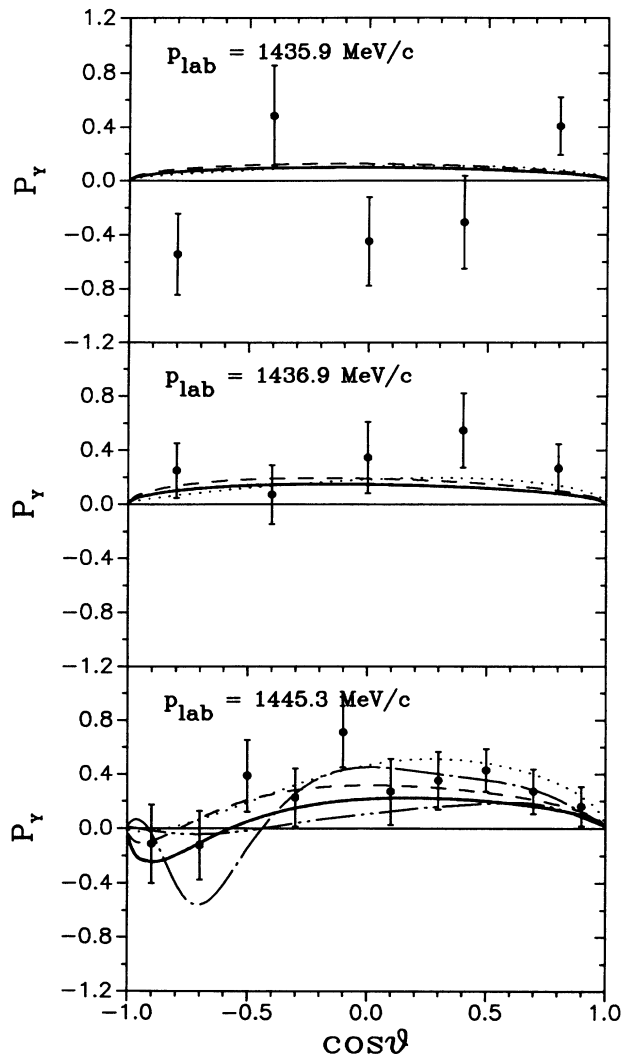


FIG. 8. Polarizations resulting from the $\bar{p}p \rightarrow \bar{\Lambda}\Lambda$ reaction near threshold. Same description of the curves as in Fig. 6. The solid line is the result of our model I. Experimental data are from Ref. [29].

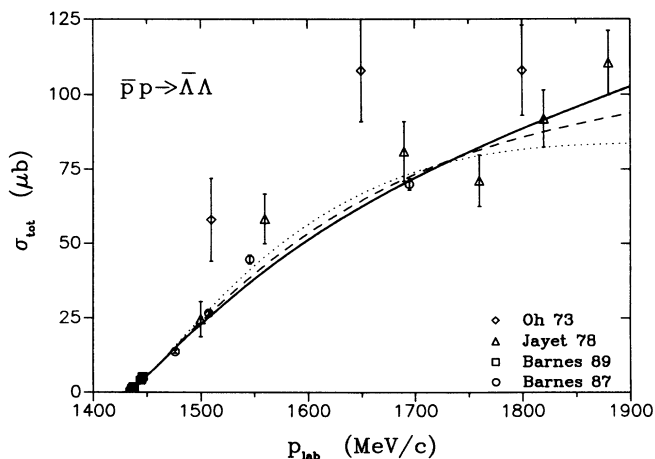


FIG. 9. Total $\bar{p}p \rightarrow \bar{\Lambda}\Lambda$ cross sections at higher energies. Same description of the curves as in Fig. 5. Experimental data are from Refs. [27] (circles), [28] (squares), [30] (downward triangles), and [31] (upward triangles).

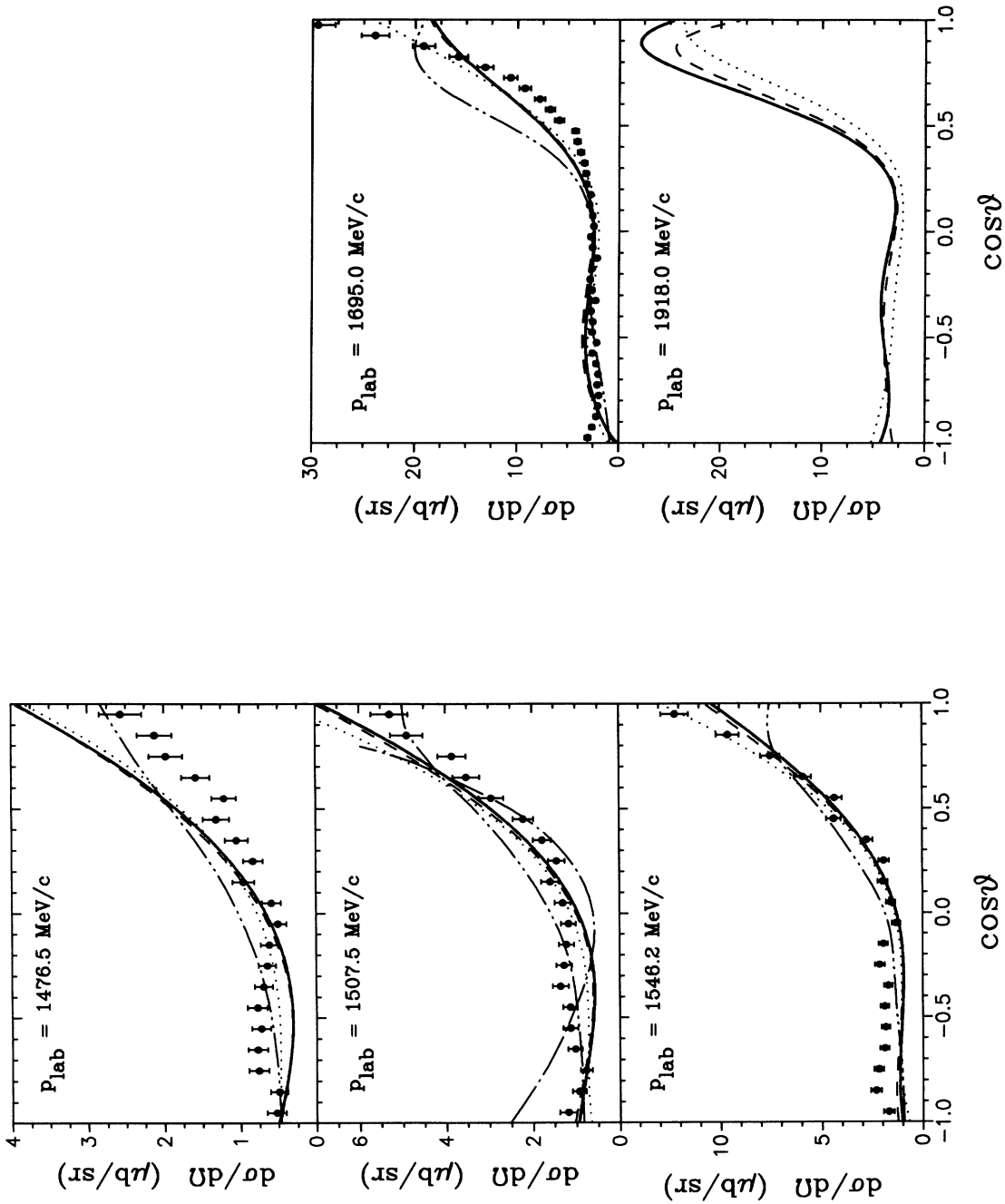


FIG. 10. Differential $\bar{p}p \rightarrow \bar{\Lambda}\Lambda$ cross sections. Same description of the curves as in Fig. 6. The solid lines indicate the results of our model I. Experimental data are from Ref. [27] ($p_{\text{lab}} = 1476.5$ and 1507.5 MeV/c) and Ref. [32] ($p_{\text{lab}} = 1546.2$ and 1695 MeV/c).

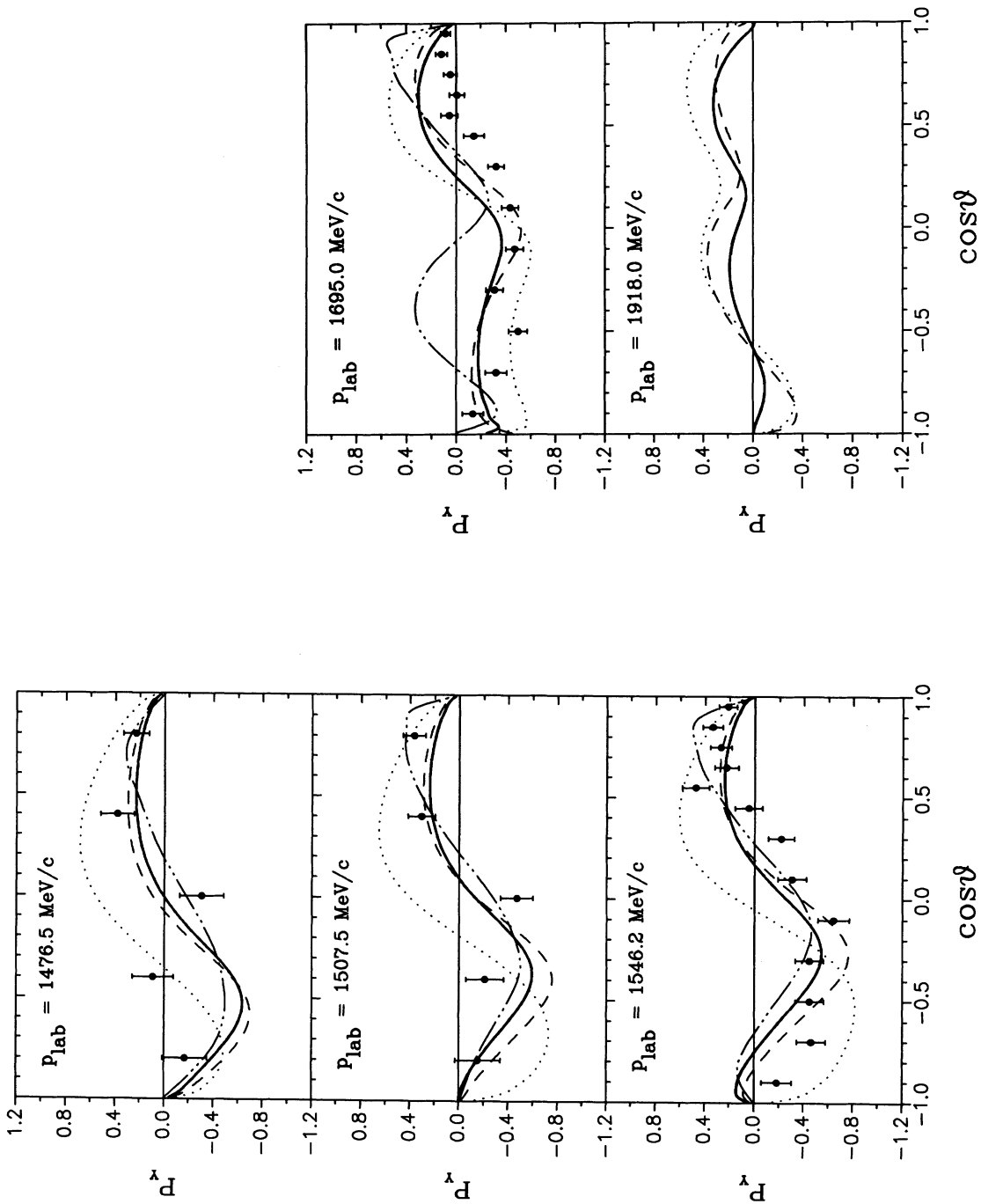


FIG. 11. Polarizations resulting from the $\bar{p}p \rightarrow \bar{\Lambda}\Lambda$ reaction. Same description of the curves as in Fig. 6. The solid lines are the result of our model I and the dash-double dotted lines the results of LL [2]. Experimental data are from Ref. [27] ($P_{\text{lab}} = 1476.5$ and 1507.5 MeV/c) and Ref. [32] ($P_{\text{lab}} = 1546.2$ and 1695 MeV/c). A preliminary analysis of the experimental data of $P_{\text{lab}} = 1918$ MeV/c indicates that P_y is essentially negative [34] and shows an angular distribution similar to $P_{\text{lab}} = 1695$ MeV/c.

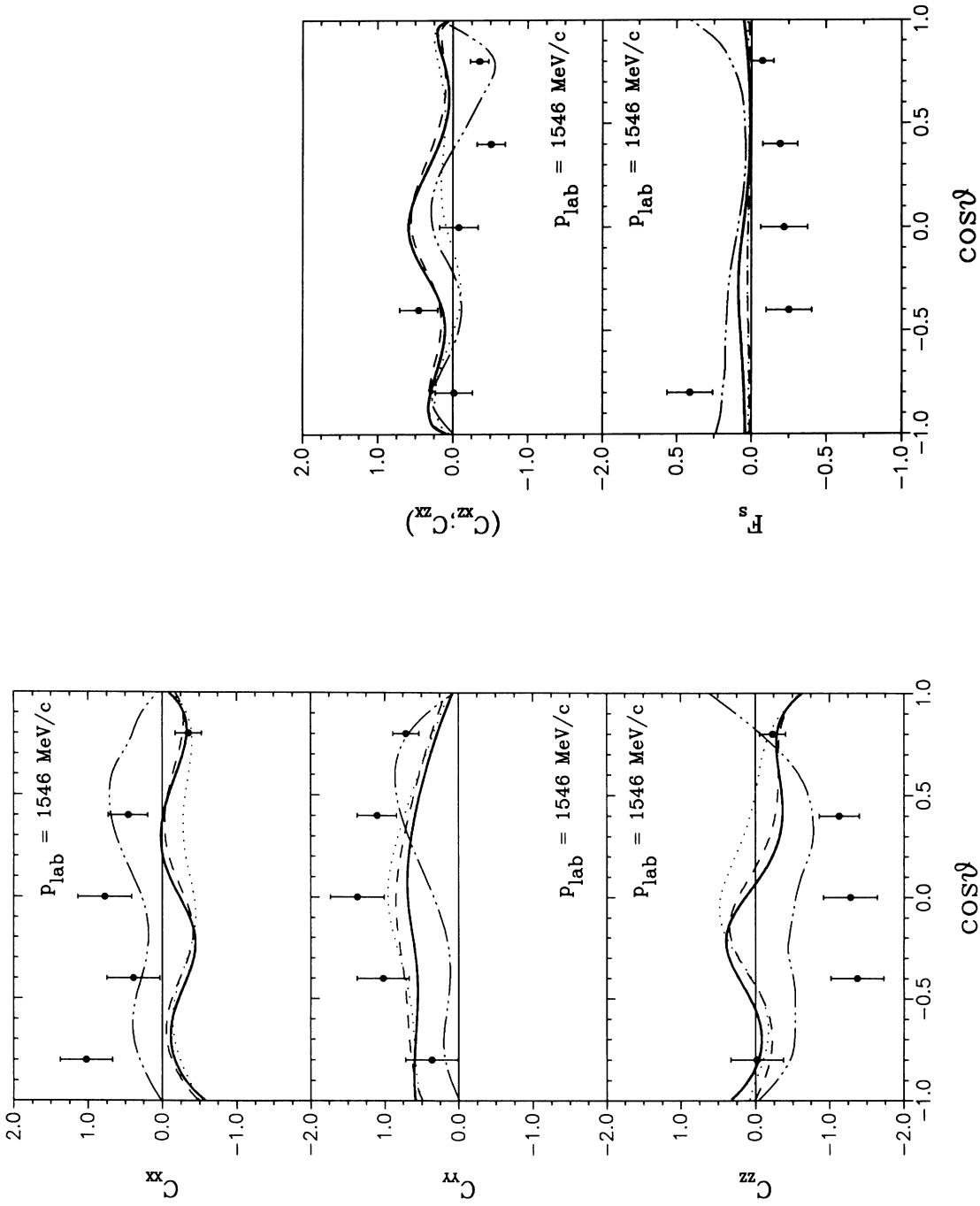


FIG. 12. Spin-correlation coefficients C_{xx}, C_{yy}, C_{zz} , mean value of C_{xz} and C_{zx} , and singlet fraction F_3 [Eq. (2.8)], for $p_{\text{lab}} = 1546 \text{ MeV}/c$. Same description of the curves as in Fig. 6. The solid lines show the results of our model I. Experimental data are from Ref. [32].

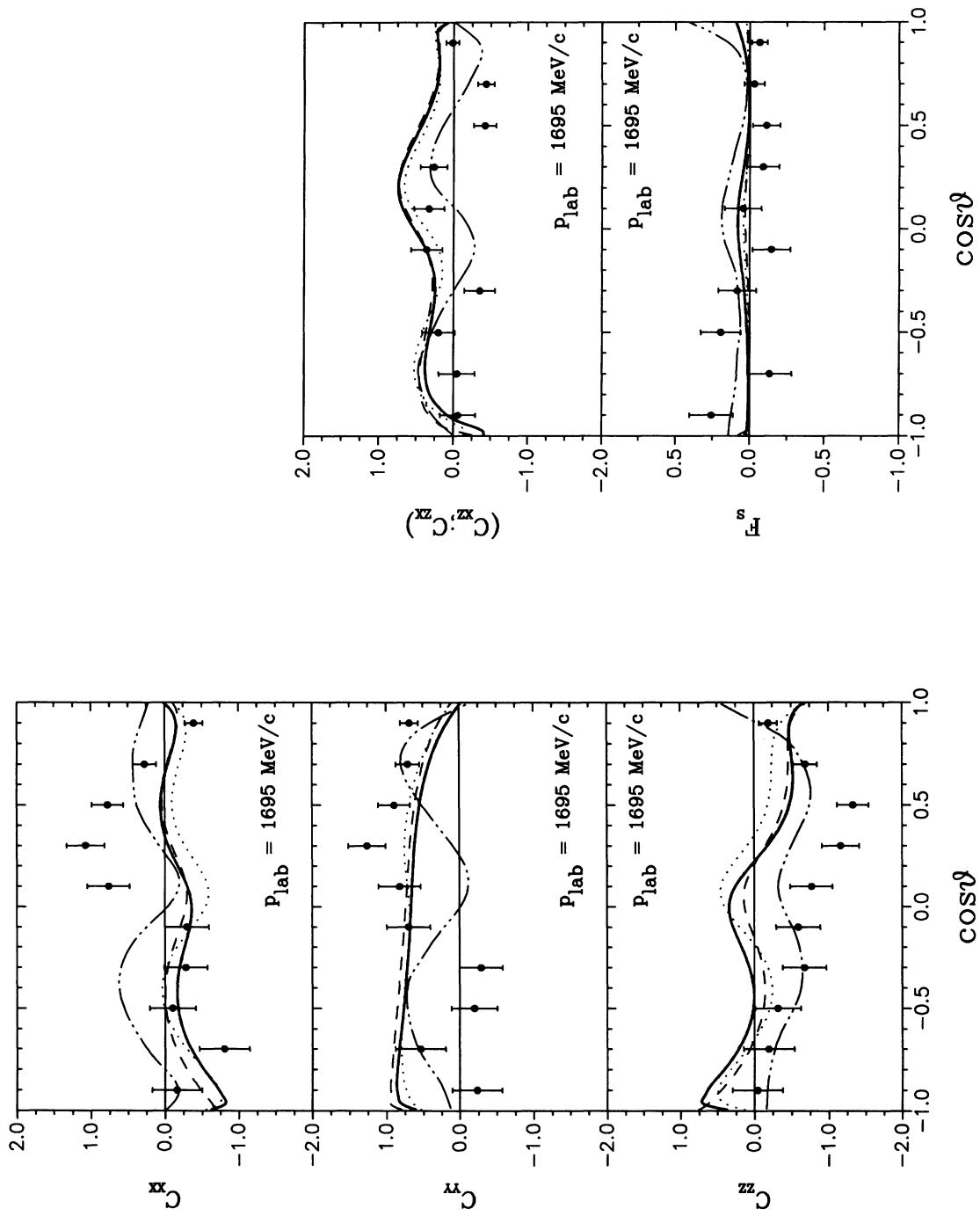
FIG. 13. Same as in Fig. 12, for $P_{\text{lab}} = 1695 \text{ MeV}/c$.

TABLE IV. Total cross sections (in μb) in the $\bar{p}p \rightarrow \bar{\Lambda}\Lambda$ channel, for various laboratory momenta (in MeV/c) and models I, II, and III described in the text. Columns II' and III' show the results based on the ingredients of models II and III, however, with $\bar{\Lambda}\Lambda$ optical potential parameters kept exactly the same as for model I.

p_{lab}	I	II	III	II'	III'
1435.9	1.0	1.0	1.0	2.2	0.4
1450.0	6.0	6.0	6.0	10.6	3.2
1500.0	22.8	23.6	24.8	34.5	15.7
1550.0	38.0	39.7	42.5	55.4	27.2
1600.0	52.0	54.2	56.8	74.0	37.0
1650.0	63.5	65.7	67.6	89.4	44.5
1700.0	72.0	73.1	74.3	100.2	49.3

1. Dominance of the spin-triplet configurations

In our meson-exchange model for the $\bar{p}p \rightarrow \bar{\Lambda}\Lambda$ transition, there is constructive interference of K and K^* exchange in the tensor channel, whereas the corresponding central potentials are essentially canceled. Therefore, the tensor part, which acts only in triplet states, dominates strongly, and the partial cross sections in the singlet channels contribute by a few percent only (see Table V). Also, for the same reason, the singlet fraction [Eq. (2.8)] at $p_{\text{lab}} = 1546 \text{ MeV}/c$ (Fig. 12) and $1695 \text{ MeV}/c$ (Fig. 13) is rather small.

In a model with kaon exchange only, the tensor force is considerably reduced, especially if the transition potential is truncated in the inner region as done by the authors of Refs. [1,2]. Consequently, the singlet fraction should become larger. This is clearly seen in the singlet fractions shown in Figs. 12 and 13, if we compare our results with those obtained by LaFrance and Loiseau [2]. In fact, the discrepancy is much larger at threshold (see Fig. 15): Whereas the predictions of our models remain quite small, the LL result for F_s is almost 0.5.

It is instructive that we can roughly reproduce the LL result by switching the sign of our K^* contribution (together with a readjustment of optical-model parameters in the $\bar{\Lambda}\Lambda$ channel). Obviously, the K^* meson, opposite

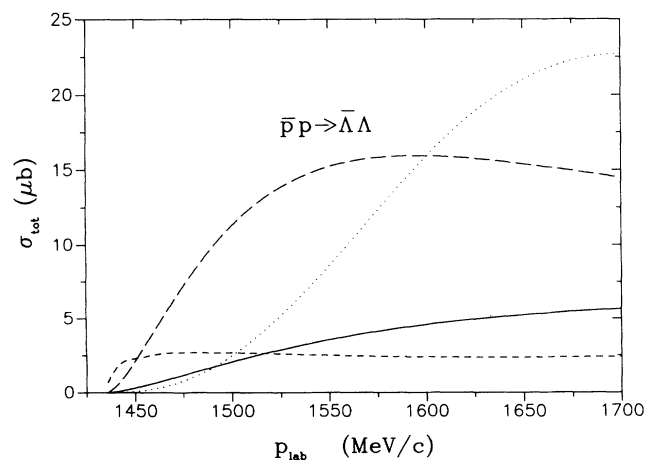


FIG. 14. Four largest (at low energies) partial-wave contributions to the total $\bar{p}p \rightarrow \bar{\Lambda}\Lambda$ cross section. The solid line belongs to the diagonal 3P_0 contribution, whereas the short-dashed, long-dashed, and dotted lines belong to the nondiagonal ${}^3D_1 \rightarrow {}^3S_1$, ${}^3F_2 \rightarrow {}^3P_2$, and ${}^3G_3 \rightarrow {}^3D_3$ transitions, respectively.

to its physical property, then simulates the strong cutoff to the K -meson contribution applied in Ref. [2].

This artificial model, providing a rather weak tensor force, but a strong central part, is also very similar to the transition potential predicted by the constituent quark model. Nevertheless, the resulting singlet fraction is quite different, namely, identically zero. By construction, the 3S_1 and 3P_0 models act as a “triplet filter” for the strange quarks. Because of the Pauli principle, the two spectator quarks in the Λ have to be in a spin-singlet state; therefore, these models act as a triplet filter also for the $\bar{\Lambda}\Lambda$ system itself.

In summary, both our meson-exchange model based on $K + K^*$ exchange and the quark-gluon models lead to

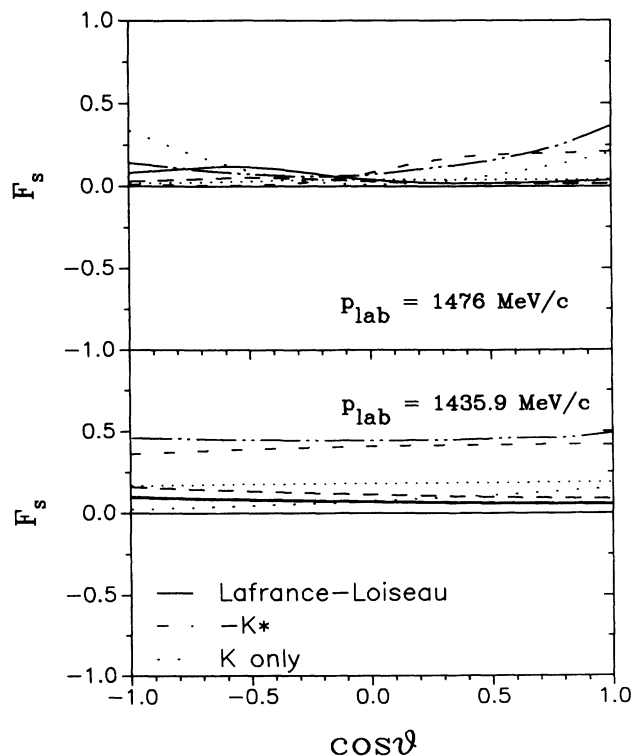


FIG. 15. Singlet fractions at the $\bar{\Lambda}\Lambda$ threshold. We compared the result of LaFrance-Loiseau [2] (dash-double dotted) and our models I (solid), II (long-dashed), and III (dotted). The short-dashed line corresponds to a calculation where we reversed the sign of the K^* -meson contribution, as discussed in the text.

TABLE V. Partial cross sections (in μb) for the $\bar{p}p \rightarrow \bar{\Lambda}\Lambda$ reaction at $p_{\text{lab}} = 1546 \text{ MeV}/c$, for our model variants I, II, III, and the Nijmegen model [4]. The total empirical cross section is $44.6 \pm 1.5 \mu\text{b}$.

	I	II	III	Nijmegen [4]
1S_0	0.2	0.2	0.4	0.2
1P_1	0.6	0.1	0.3	0.5
1D_2	0.3	0.1	0.1	0.3
3S_1	0.5	0.4	0.5	1.3
$^3D_1 \rightarrow ^3S_1$	2.5	3.7	1.4	5.1
$^3S_1 \rightarrow ^3D_1$	0.1	0.1	0.2	0.6
3D_1	2.1	1.7	1.5	
3P_0	3.5	4.7	6.4	0.4
3P_1	0.5	1.0	2.6	7.0
3P_2	1.7	1.2	1.3	3.3
$^3F_2 \rightarrow ^3P_2$	15.1	16.1	19.8	10.2
3D_3	1.0	0.7	0.8	1.4
$^3G_3 \rightarrow ^3D_3$	8.0	7.8	5.5	5.1
Total	36.2	37.9	40.7	39.5

very small singlet fractions, for completely different reasons. However, if only truncated kaon exchange is used, the singlet fraction turns out to be considerably larger, especially at low energies.

2. *P*-wave dominance near the $\bar{\Lambda}\Lambda$ threshold

Usually, the observed *P*-wave dominance is achieved by a suppression of the *S* waves in the $\bar{\Lambda}\Lambda$ channel with the help of a suitable optical potential. In the following we will describe in some detail how this arises in either meson-exchange or constituent quark models.

We have already seen in Fig. 14 that in our model based on *K*- and *K**-meson exchange the $\Delta L = -2$ tensor transitions essentially describe the $\bar{p}p \rightarrow \bar{\Lambda}\Lambda$ process. Because of the angular momentum barrier being quite effective at low energies, the $^3D_1 \rightarrow ^3S_1$ transition is largest just at threshold; however, the $^3F_2 \rightarrow ^3P_2$ wave soon takes over and dominates the process already at a momentum of about 15 MeV/*c* above threshold, in agreement with experiment (cf. Fig. 7).

In our model this characteristic feature comes about in the following way: As Fig. 16(a) demonstrates, the relevant partial waves in the $\bar{p}p$ entrance channel, 3D_1 and 3F_2 , have about the same strength. Because of the angular momentum barrier, however, the $^3D_1 \rightarrow ^3S_1$ transition is strongly favored in the $\bar{\Lambda}\Lambda$ channel at low energies: Without the $\bar{\Lambda}\Lambda$ final-state interaction, this partial wave dominates for momenta up to 1530 MeV/*c*, much larger than empirically observed, as shown in Fig. 16(b) (upper solid line). The $\bar{\Lambda}\Lambda$ final-state interaction now reduces the $^3D_1 \rightarrow ^3S_1$ wave strongly (lower solid line), but keeps the $^3F_2 \rightarrow ^3P_2$ wave (dashed lines) essentially unchanged, at least near threshold, because, as a result of the very low relative momentum, the $\bar{\Lambda}$ and Λ baryons have to be far apart in order to gain one unit of orbital angular momentum.

In the constituent quark model, one arrives at essentially the same result: Again, the angular momentum barrier favors the lowest partial waves, which are then suppressed by a suitable $\bar{\Lambda}\Lambda$ optical potential. Also, the

$\bar{\Lambda}\Lambda$ system near threshold is preferably in a 3P_2 state, however, for a different physical reason: Now the tensor part in the transition potential is negligibly small; therefore, the process is governed by diagonal ($\Delta L = 0$) transitions. As seen in Fig. 16(a), the 3P_2 wave is by far the strongest in the entrance channel: the central transition potential keeps this behavior also in the final channel.

Alternatively, *P*-wave dominance can also be obtained by enhancing the *P* waves by means of *P*-wave resonances close at threshold. Dalkarov, Protasov, and Shapiro [33] have used this phenomenon, together with a transition potential based on *K*-meson exchange and in a (phenomenological) coupled-channel framework. By suitable adjustments of parameters in the transition and coupled-channel potentials, they were able to reproduce the total and differential cross sections as well as the *polarization* data near threshold. However, since the authors have omitted the important tensor contribution in their transition potential, the resulting singlet fraction should be substantially larger than in other models, throughout the whole energy range.

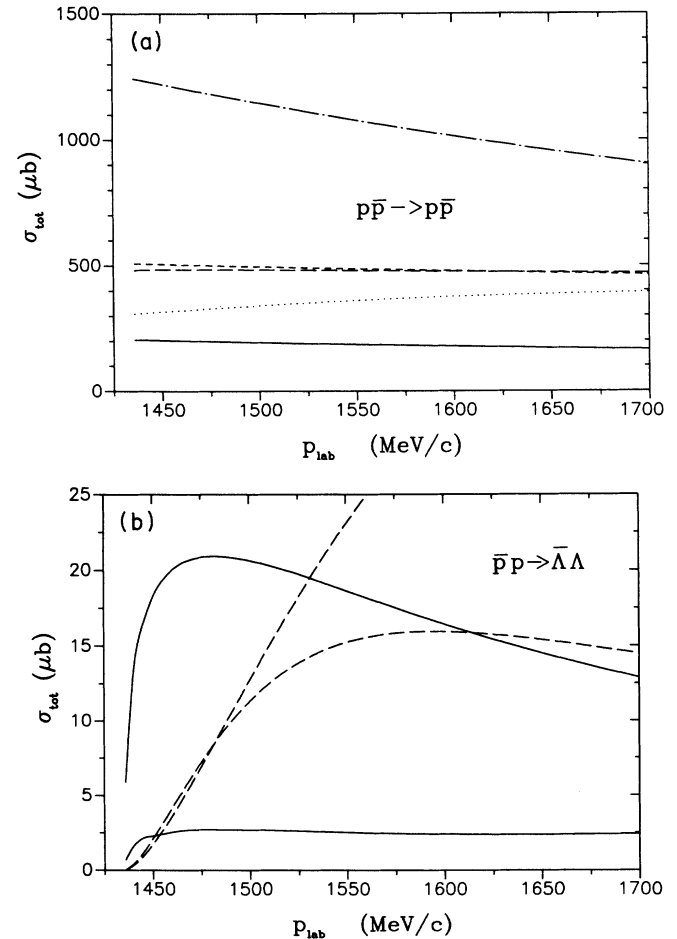


FIG. 16. (a) Selected partial-wave contributions to the total $\bar{p}p \rightarrow \bar{p}p$ cross section. (Solid line, 3P_0 ; short-dashed, 3D_1 ; long-dashed, 3F_2 ; dotted, 3G_3 ; and dash-dotted, 3P_2). (b) Two strongest partial-wave contributions (solid line, $^3D_1 \rightarrow ^3S_1$; dashed line, $^3F_2 \rightarrow ^3P_2$) to the total $\bar{p}p \rightarrow \bar{\Lambda}\Lambda$ cross section. The upper part of each line corresponds to the results where no optical potential acts in the $\bar{\Lambda}\Lambda$ channel.

In summary, all models can account for the observed P -wave dominance near threshold, but for quite different physical reasons. We expect, however, that differences should show up at higher energies. Therefore, it is important to compare the corresponding results with all the existing data and not only at one energy, but over a large energy range.

3. How to distinguish the models

We have seen that both meson-exchange and constituent quark models are able to explain the basic qualitative features of the $\bar{p}p \rightarrow \bar{\Lambda}\Lambda$ reaction, namely, the dominance of (i) spin-triplet configurations and (ii) P waves near the $\bar{\Lambda}\Lambda$ threshold. Moreover, cross-section as well as polarization data can be reasonably reproduced in both scenarios, at least near threshold. One reason is that the $\bar{\Lambda}\Lambda$ final-state interaction is not known empirically or sufficiently constrained theoretically, at least in the annihilation part. This freedom can be used to suitably adjust the $\bar{\Lambda}\Lambda$ optical potential in both cases.

However, the underlying physical mechanisms are quite different in both scenarios: In the meson-exchange model, the $\Delta L = -2$ transitions, induced by the strong tensor force due to $(K + K^*)$ exchange, dominate the partial waves in the $\bar{\Lambda}\Lambda$ channel. Such transitions are forbidden (3S_1 version) or strongly suppressed (3P_0 version) in the constituent quark models. Although this difference is expected to have some impact on the results, especially as far as the energy dependence is concerned, a more direct distinction would be provided by spin-transfer data. If the transitions are mainly connected with a spin flip, the meson-exchange model is the appropriate description; if not, the constituent quark model is more suitable.

E. Predictions for the $\bar{\Lambda}\Lambda$ channel

For all three model variants, the coupled-channel framework provides definite predictions for observables

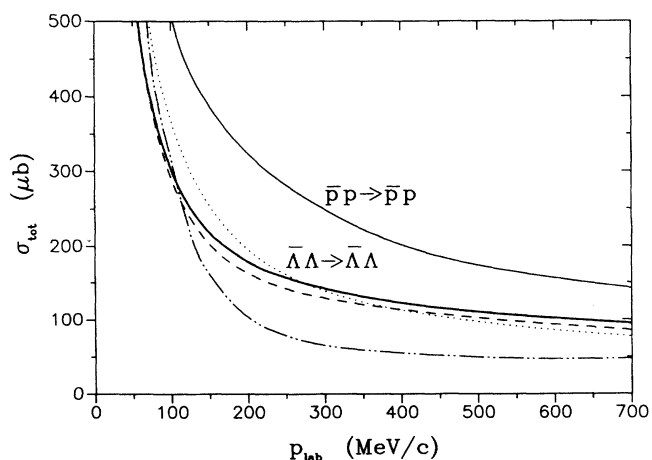


FIG. 17. Total $\bar{\Lambda}\Lambda \rightarrow \bar{\Lambda}\Lambda$ cross sections as function of the Λ laboratory momentum. Same description of the curves as in Fig. 6. The $\bar{p}p \rightarrow \bar{p}p$ curve, at the same laboratory momentum, is taken from our low-energy $\bar{p}p$ model A (box) [16].

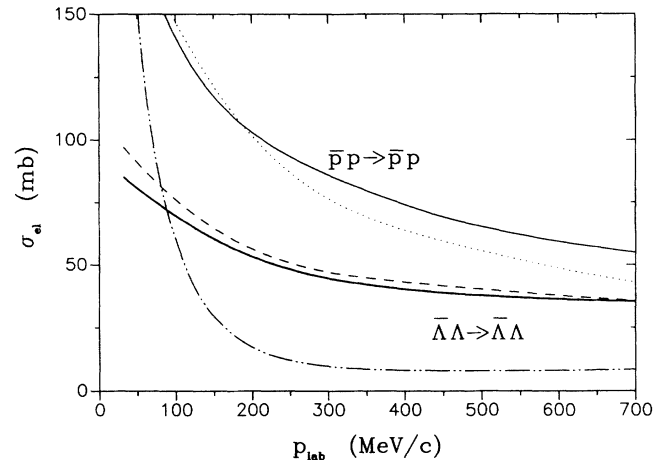


FIG. 18. Same as in Fig. 15, for the elastic $\bar{\Lambda}\Lambda \rightarrow \bar{\Lambda}\Lambda$ cross sections.

in the diagonal $\bar{\Lambda}\Lambda$ channel. Corresponding results are shown in Fig. 17 for the total cross section. Surprisingly enough, all our models yield essentially the same results. Note, however, that our predictions are about a factor of 2 larger (at higher momenta) than corresponding results given by LaFrance and Loiseau [2]. The discrepancy is even more drastic for the elastic cross sections shown in Fig. 18. Here our model III also differs somewhat from the results for models I and II, which are still very similar. Concerning the ratio σ_{tot}/σ_{el} , our models yield roughly a factor of 2, whereas it is as large as 5 in case of the LaFrance-Loiseau model [2]. As seen also from the

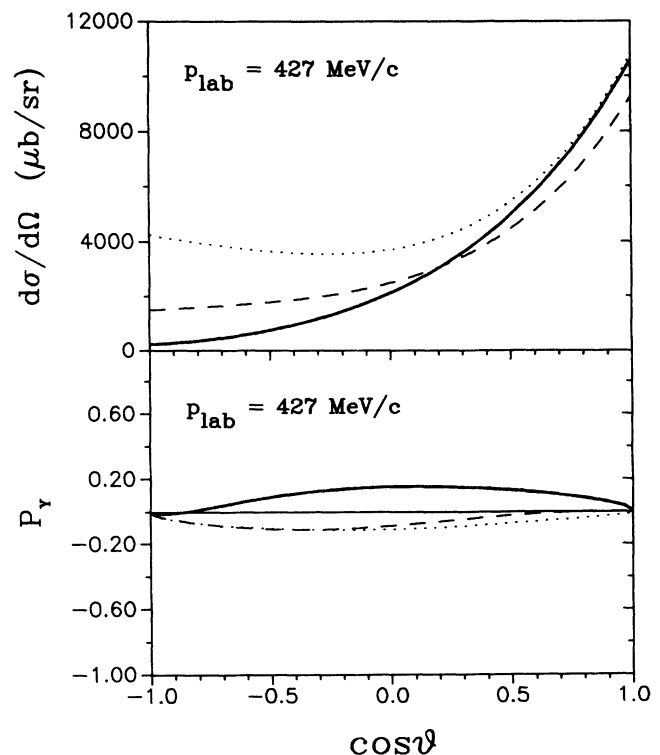


FIG. 19. Differential cross section and polarization in the $\bar{\Lambda}\Lambda \rightarrow \bar{\Lambda}\Lambda$ channel, for a Λ laboratory momentum of 427 MeV/c. Same description of the curves as in Fig. 6.

figures, the corresponding $\bar{p}p$ results in the same momentum range (i.e., $p_{\text{lab}}^{\bar{p}} = p_{\text{lab}}^{\Lambda}$) are considerably larger since both the elastic part (due to larger meson-baryon coupling constants) and the annihilation part (because of the larger range) are much stronger.

A similar situation occurs for the $\bar{\Lambda}\Lambda$ differential cross sections and polarizations, shown in Fig. 19 $p_{\text{lab}}^{\Lambda} = 427$ MeV/c. The differences between our model predictions are non-negligible.

In our opinion the results of this section lead to the conclusion that, given the present uncertainties in the theoretical treatment, the possibilities for making a reliable and unambiguous prediction for $\bar{\Lambda}\Lambda$ observables by fixing open parameters in the $\bar{p}p \rightarrow \bar{\Lambda}\Lambda$ channel are very limited.

IV. SUMMARY

In this paper we have studied the strangeness production process $\bar{p}p \rightarrow \bar{\Lambda}\Lambda$ at threshold and intermediate energies in a full coupled-channel ($\bar{p}p, \bar{\Lambda}\Lambda$) calculation. The elastic part of the diagonal interactions has been constructed from a one-boson-exchange version of the Bonn NN potential and a corresponding extension to the hyperon-nucleon case, whereas the annihilation part is parametrized by simple phenomenological optical potentials in both $\bar{p}p$ and $\bar{\Lambda}\Lambda$ channels. The transition interaction is based on K^* as well as K exchange. It was possible to take both coupling constants and cutoff masses to be precisely the same as in our hyperon-nucleon model [13]; i.e., no additional *ad hoc* regularization was introduced. This is important since only through a combined and consistent description of many hadronic reactions one will have a chance to possibly detect deficiencies in the conventional picture.

We obtain a good reproduction of the empirical $\bar{p}p \rightarrow \bar{\Lambda}\Lambda$ data. In our model the reaction is dominated by transitions $L_{\bar{\Lambda}\Lambda} = L_{\bar{p}p} - 2$, generated by the strong tensor force due to combined ($K + K^*$) exchange. (In contrast, quark-gluon models provide a strong central, but a weak tensor force.) Furthermore, because of the relatively large kinetic energy in the initial $\bar{p}p$ state, the centrifugal barrier is much less effective here; consequently, contributions from higher partial waves (even G waves) become

quite important.

Our coupled-channel model automatically yields results for the observables in the diagonal $\bar{\Lambda}\Lambda$ channel, for which there exist no measurements. Unfortunately, with the present uncertainties in the theoretical treatment, it is not possible, at least at present, to make unambiguous predictions. In this connection it is important to note that, in contrast to claims made sometimes by other groups, the results in the $\bar{p}p \rightarrow \bar{\Lambda}\Lambda$ channel do depend sensitively on modifications in the short-range part of the transition interaction, in spite of the strong annihilation present in the initial and final states. In principle, this fact would allow discrimination between various pictures of the dynamics of the transition; however, with the freedom in the choice of phenomenological optical-model parameters for the final-state annihilation, this is rather limited at present. Nevertheless, in view of the strongly different size of the tensor force in the $\bar{p}p \rightarrow \bar{\Lambda}\Lambda$ transition for the meson or quark-gluon scenario, there is good reason to expect that some differences will show up in the energy dependence of the polarization data. A more direct information about the validity of either scenario would be provided by spin-transfer data since the amount of spin-flip transitions is strongly correlated to the size of the tensor force in the transition interaction. On the other hand, it is our firm belief that ultimately a consistent microscopic model, also for the annihilation part, will inevitably be required in order to obtain a reliable and theoretically well-founded dynamical model for this reaction.

Note added in proof: We just learned from B. Loiseau that their results published in Ref. [2] for the diagonal $\bar{\Lambda}\Lambda$ interaction are not correct. Accordingly, their result in Fig. 17 (18) should be multiplied with a factor of 2 (4). The differences to our models then become much less pronounced.

ACKNOWLEDGMENTS

Thanks are due to E. Lomon for numerous suggestions concerning the manuscript and K. Kilian and W. Oelert for many discussions. This work was supported in part by the Australian Research Council and by NATO Collaborative Research Grant No. 850093.

-
- [1] M. Kohno and W. Weise, Phys. Lett. B **179**, 15 (1986); **206**, 584 (1988); Nucl. Phys. A**479**, 433c (1988).
- [2] P. LaFrance, B. Loiseau, and R. Vinh Mau, Phys. Lett. B **214**, 317 (1988); in *Physics at LEAR with Low Energy Antiprotons, Proceedings of the IV Lear Workshop*, edited by C. Amsler *et al.* (Harwood Academic, New York, 1988), p. 375; P. LaFrance and B. Loiseau, Nucl. Phys. A**528** 557 (1991); in *Proceedings of the First Biennial Conference on Low Energy Antiproton Physics, Stockholm, Sweden, 1990*, edited by P. Carlson, A. Karek, and S. Szilagy (World Scientific, Singapore, 1991), p. 122.
- [3] J. A. Niskanen, Report No. HU-TFT-85-28, University of Helsinki, 1985.
- [4] R. G. E. Timmermanns, T. A. Rijken, and J. J. de Swart, Nucl. Phys. A**479**, 383c (1988); in *Physics at LEAR with Low Energy Antiprotons* [2], p. 357.
- [5] F. Tabakin and R. A. Eisenstein, Phys. Rev. C **31**, 1857 (1985).
- [6] B. Holzenkamp, T. Hippchen, K. Holinde, and J. Speth, IKP Annual Report 1988; Jül-Spez **499**, 109 (1989); in Book of Contributions to the 12th International Conference on Few-Body Systems in Physics, TRIUMF Report No. TRI-89-2, Vancouver, 1989, p. 114.
- [7] H. Genz and S. Tatur, Phys. Rev. D **30**, 63 (1984); G. Brix, H. Genz, and S. Tatur, *ibid.* **39**, 2054 (1989).
- [8] H. R. Rubinstein and H. Snellman, Phys. Lett. **165B**, 187 (1985).
- [9] S. Furui and A. Fässler, Nucl. Phys. A**468**, 669 (1987).
- [10] P. Kroll and W. Schweiger, Nucl. Phys. A**474**, 608 (1987); in *Physics at LEAR with Low Energy Antiprotons* [2], p.

- 353; P. Kroll, B. Quadder, and W. Schweiger, Nucl. Phys. **B316**, 373 (1989).
- [11] M. A. Alberg, E. M. Henley, and L. Wilets, Z. Phys. A **331**, 207 (1988); Phys. Rev. C **38**, 1506 (1988); M. A. Alberg, K. Braeuer, E. M. Henley, and L. Wilets, in *Physics at LEAR with Low Energy Antiprotons* [2], p. 361; M. A. Alberg, E. M. Henley, P. D. Kunz, and L. Wilets, in *Proceedings of the First Biennial Conference on Low Energy Antiproton Physics* [2], p. 129; M. A. Alberg, E. M. Henley, L. Wilets, and P. D. Kunz, Nucl. Phys. **A508**, 323c (1990).
- [12] M. Burkardt and M. Dillig, Phys. Rev. C **37**, 1362 (1988).
- [13] B. Holzenkamp, K. Holinde, and J. Speth, Nucl. Phys. **A500**, 485 (1989).
- [14] J. Haidenbauer, K. Holinde, and M. B. Johnson, Phys. Rev. C (to be published).
- [15] R. Machleidt, K. Holinde, and Ch. Elster, Phys. Rep. **149**, 1 (1987).
- [16] J. Haidenbauer, T. Hippchen, K. Holinde, and J. Speth, Z. Phys. A **334**, 467 (1989); J. Haidenbauer, T. Hippchen, and K. Holinde, Nucl. Phys. **A508**, 329c (1990); T. Hippchen, J. Haidenbauer, K. Holinde, and V. Mull, Phys. Rev. C **44**, 1323 (1991); V. Mull, J. Haidenbauer, T. Hippchen, and K. Holinde, Phys. Rev. C **44**, 1337 (1991).
- [17] M. M. Nagels, T. A. Rijken, and J. D. de Swart, Phys. Rev. D **17**, 768 (1978); **20**, 1633 (1979).
- [18] M. Lacombe *et al.*, Phys. Rev. C **21**, 861 (1980).
- [19] J. Haidenbauer, K. Holinde, and A. W. Thomas, Phys. Rev. C **45**, 952 (1992), this issue.
- [20] R. J. Abrams *et al.*, Phys. Rev. D **1**, 1917 (1970).
- [21] M. Coupland, E. Eisenhandler, W. R. Gibson, P. I. P. Kalmus, and A. Astbury, Phys. Lett. **71B**, 460 (1977).
- [22] D. L. Parker, B. Y. Oh, G. A. Smith, and R. J. Sprafka, Nucl. Phys. **B32**, 29 (1971).
- [23] D. Cutts *et al.*, Phys. Rev. D **17**, 16 (1978).
- [24] E. Eisenhandler *et al.*, Nucl. Phys. **B113**, 1 (1976).
- [25] R. A. Kunne *et al.*, Nucl. Phys. **B323**, 1 (1989).
- [26] C. Daum, F. C. Ern , J. P. Lagnaux, J. C. Sens, M. Steuer, and F. Udo, Nucl. Phys. **B6**, 617 (1968).
- [27] P. D. Barnes *et al.*, Phys. Lett. B **189**, 249 (1987).
- [28] P. D. Barnes *et al.*, Phys. Lett. B **229**, 432 (1989).
- [29] R. v. Frankenberg *et al.*, in *Physics at LEAR with Low Energy Antiprotons* [2], p. 347.
- [30] B. Y. Oh *et al.*, Nucl. Phys. **B51**, 57 (1973).
- [31] B. Jayet *et al.*, Nuovo Cimento A **45**, 371 (1978).
- [32] P. D. Barnes *et al.*, Nucl. Phys. **A526**, 575 (1991).
- [33] O. D. Dalkarov, K. V. Protasov, and I. S. Shapiro, Int. J. Mod. Phys. A **5**, 2155 (1990).
- [34] W. Oeler (private communication).